Research article

Longtao Wang, Jiangtao Xu, Jiafeng Lu, Linping Teng, Zhengqian Luo, Fufei Pang and Xianglong Zeng*

3 W average-power high-order mode pulse in dissipative soliton resonance mode-locked fiber laser

https://doi.org/10.1515/nanoph-2021-0317
Received June 23, 2021; accepted August 13, 2021; published online August 31, 2021

Abstract: Recently high-order modes (HOMs) lasers have been extensively investigated due to their potential applications in mode-division multiplexing. In this paper, we present two schemes of generating HOMs from the mode-locked fiber lasers (MLFLs) in the dissipative soliton resonance (DSR) regime. Watt-level HOM outputs are implemented through intra-cavity mode conversion. 3 W average-power HOMs with an efficiency slope of 25% can be obtained based on an MLFL in the DSR regime, which is achieved by incorporating a long-period fiber grating (LPFG) and a dual-resonant acoustically induced fiber grating (AIFG), respectively. Their different spectrum responses enable flexible mode conversion in the MLFLs. Both fiber mode converters are exploited to show their robust capability of efficient mode manipulation. The MLFL with an LPFG inserted in the cavity can achieve wide-bandwidth intra-cavity optical vortex beams (OVBs) near the dispersion turning around point because of the pulses of the fundamental mode and high-order vortex eigenmodes oscillating in the cavity with the same group velocity to form spatio-temporal mode locking. The MLFL based on a dual-resonant AIFG can perform the function of fast switching (~0.3 ms) in LP_{01}, LP_{11a}, and LP_{11b} modes with a high modal purity of 96%. These different modes with high-energy pulses can be flexibly switched with programmable radio frequency modulation. Furthermore, a quarter-wave plate and a polarizer are employed at the output of fiber laser to realize the controllability of the mode field, which is possible to generate a controllable mode field of OVBs based on the first-order Poincaré sphere. This control method can be integrated with the MLFLs to extend the flexibility of high-power HOMs generation.

Keywords: acoustically induced fiber grating; dissipative soliton resonance; high-order modes; long period fiber grating; mode-locked fiber laser.

1 Introduction

Optical pulses with extremely high energy are of great significance to the development of advanced experimental platforms and industrial tools. The light field has dramatically increased by advancing the techniques of mode-locked fiber lasers (MLFLs), which have been widely investigated due to their potential application in laser micromachining [1, 2], optical sensing [3] and biomedical imaging [4], etc. Watt-level pulse power can be obtained from an MLFL in the dissipative soliton resonance (DSR) regime, which is theoretically predicted by Akhmediev et al. [5, 6]. The features of a DSR mode-locked pulse are: (1) the pulse duration increases with the pump power and (2) the pulse amplitude keeps at a constant level. Theoretically, the pulse energy can be amplified indefinitely without optical wave breaking. Thus, the MLFLs working in the DSR region become an ideal platform for exploiting the characteristics of high-power pulses.

Most of the MLFLs using the fundamental mode in fibers have been constructed and investigated both in the

Longtao Wang and Jiangtao Xu have contributed to this work equally.

***Corresponding author: Xianglong Zeng**, The Key Lab of Specialty Fiber Optics and Optical Access Network, Joint International Research Laboratory of Specialty Fiber Optics and Advanced Communication, Shanghai University, Shanghai 200444, China,
E-mail: zenglong@shu.edu.cn. https://orcid.org/0000-0001-7817-173X
Longtao Wang, Jiangtao Xu, Jiafeng Lu, Linping Teng and Fufei Pang, The Key Lab of Specialty Fiber Optics and Optical Access Network, Joint International Research Laboratory of Specialty Fiber Optics and Advanced Communication, Shanghai University, Shanghai 200444, China. https://orcid.org/0000-0002-0778-7657 (L. Wang). https://orcid.org/0000-0002-2691-6688 (J. Lu). https://orcid.org/0000-0002-7106-4584 (F. Pang)
Zhengqian Luo, Department of Electronic Engineering, Xiamen University, Xiamen 361005, China. https://orcid.org/0000-0002-2800-8472

laser theory and practical applications [7–10]. However, the limitation of single-mode fiber (SMF) in transmission capacity cannot be ignored with the increasing demand for data volume. The emergence of optical space division multiplexing (SDM) technology provides a reliable means to solve the capacity crisis [11, 12]. The few-mode fibers (FMFs) and multimode fibers (MMFs) propagating multiple core modes have become the carriers of SDM technology. These modes in FMFs and MMFs exhibit different spatial distributions and interact with each other in ultrafast nonlinear optics, thus eventually evolve into spatiotemporal MLFLs [13–17].

High-order mode (HOM) pulses from an all-fiber MLFL have attracted a lot of attention due to their unique spatial intensity and polarization distribution properties [18–24]. However, a single LP_{11} mode state in the FMF has been demonstrated in the fiber lasers [25, 26]. Dong et al. [27] reported an MLFL that inserts a two-mode fiber (TMF) Bragg grating (FBG) for transverse-mode conversion in 2014, but it is noted that the narrow reflection bandwidth of FBG limits the bandwidth of HOM pulses. In 2017, Wang et al. [28] achieved the generation of HOM pulses in all-fiber MLFL using a mode selective coupler. But generating HOM pulses is always limited by the laser power available in the mode-locking mechanism, such as nonlinear polarization rotation (NPR), nonlinear optical loop mirror/nonlinear amplifying loop mirror (NOLM/NALM), saturable absorber, etc., in which excess nonlinear effect would lead to optical wave breaking. Therefore, the pulse power is typically limited to less than hundreds of mW. There is no relevant report on the mode-locked pulses of generating high-power HOMs and no consideration about the stability of spatial mode with high power by using DSR mode-locking to our knowledge.

In this paper, we introduce two important all-fiber mode conversion devices, namely broadband long-period fiber grating (LPFG) and acoustically induced fiber grating (AIFG), which are inserted into the MLFLs to obtain the intra-cavity DSR mode-locked pulses with Watt-level HOM outputs. They have different spectral responses and enable flexible mode conversion in the MLFLs. More important, their compatibility with the SMF components used in the intra-cavity fiber lasers is highly desired. Optical oscillation of vortex pulses and dynamical switching of HOM patterns are achieved respectively by means of mode-locking in the DSR region. These results are helpful for scientists to understand the interaction of different spatial modes in the DSR regime of the mode-locked state.

The proposed MLFLs with two fiber mode converters present different features. First, stable optical vortex beams (OVBs) output based on a broadband LPFG is available in the MLFLs due to matched group velocities of eigenvector modes of LP_{11} mode. Optical vortex pulses with orbital angular momentum (OAM) oscillate through broadband mode conversion inside the cavity. Second, a dual-resonant AIFG has the function of fast switching [29–33], which enable the mode-locked pulses with different spatial $LP_{11a/b}$ mode pattern. This provides an ideal experimental platform for observing the dynamic switching of high-power pulses with different transversal modes, which can be flexibly switched with programmable radio frequency (RF) modulation.

Furthermore, based on the theory of first-order Poincaré sphere [34], a quarter-wave plate (QWP) and a polarizer are employed at the output of fiber laser to realize the controllability of the mode fields between OVBs and LP_{11} mode. This control method can be integrated with the MLFLs to extend the flexibility of high-power HOM beam generation.

2 Experimental setups and methods

2.1 DSR MLFL based on intra-cavity LPFG and AIFG

The schematic setup of an MLFL using the DSR mechanism is shown in Figure 1. In theory, the DSR in the MLFL can provide enormous pulse energy by increasing the pulse durations. Here a length of 2-m high nonlinear fiber with group velocity dispersion of 0 ps^2/m around 1550 nm is inserted in the NOLM to accumulate the nonlinear phase shift. The NOLM is made of a 5:95 optical coupler and one PC in the NOLM is used to adjust loss and nonlinear phase shift in order to obtain the mode-locking state [35]. The intensity filtering characteristics of the NOLM are used to narrow the pulse passively. The stability of the mode-locked pulse is high due to the independence of the light's polarization characteristics in such a laser cavity. A segment of 4-m Er: Yb co-doped double-clad fiber (EYDF) with group velocity dispersion of -0.019 ps^2/m around 1550 nm is pumped by a 980 nm laser diode with a 980/1550 nm optical combiner. Its peak core absorption near 1550 nm is about 95.5 dB/m. The maximum output power of a 980 nm laser diode is 12 W.

As shown in Figure 1a and b, the broadband turning around point (TAP)-LPFG and dual-resonant AIFG are inserted into the linear cavity to obtain the oscillation of LP_{11} modes, respectively. The hybrid cavity is divided into two fiber sections propagating LP_{01} and LP_{11} modes. Therefore, a mode stripper (MS) between them is exploited to ensure a pure LP_{01} mode light beam propagating in the AIFG or the

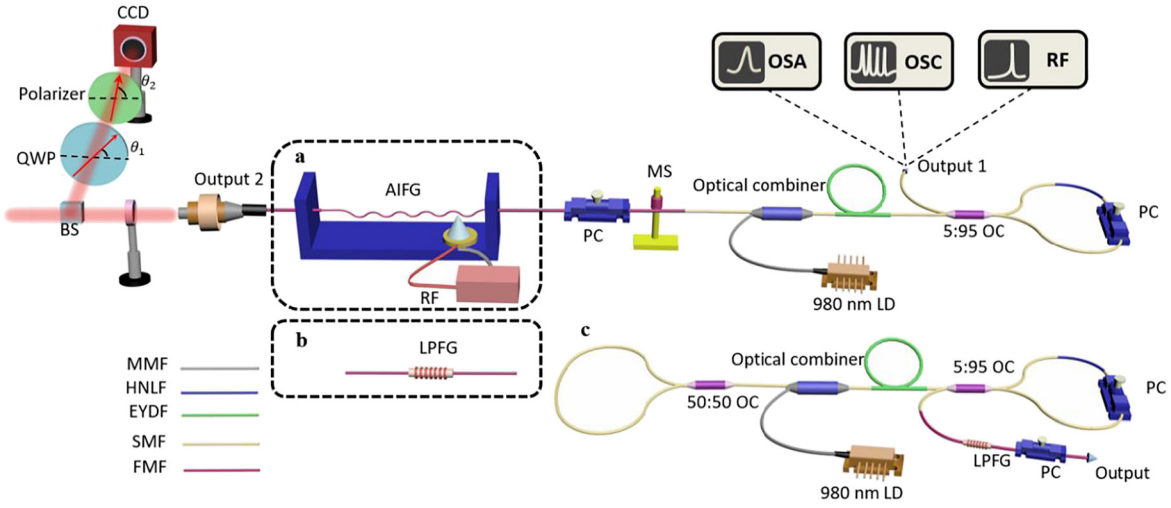

Figure 1: Experimental setup of mode-locked fiber laser used to excite intra-cavity high order mode based on (a) AIFG, (b) LPFG. (c): Experimental setup of mode-locked fiber laser used to excite extra-cavity high order mode based on LPFG. EYDF, Er: Yb Co-doped Double-clad Fiber; PC, Polarization Controller; OC, Optical Coupler; MS, mode stripper; QWP, quarter-wave plate; CCD, Charge-Coupled Device, Infrared camera. The angle between the fast axis of the QWP and the *x*-axis is θ_1. The angle between the transmission axis of the polarizer and the *x*-axis is θ_2.

LPFG, because direct splicing between the SMF and the FMF may introduce HOMs in the FMFs. The pigtailed fiber with 4% Fresnel reflectivity is used as the output mirror. The output is attenuated and collimated through a mode field control setup, which consists of a QWP and a polarizer. The pulsed LP_{11} mode can be delivered by the DSR MLFL based on the intra-cavity LPFG and AIFG. Though both act as efficient mode conversion between LP_{01} and LP_{11} modes, their different kind of spectrum responses are investigated to enable optical vortex mode-locking and dynamic HOM switching, respectively.

Meanwhile, one fiber loop mirror made of a 50:50 optical coupler is used as a highly reflective mirror to obtain the DSR mode-locked pulses of LP_{01} mode. The same LPFG acts as an extra-cavity mode converter from the output port of the NOLM in Figure 1c. An optical spectrum analyzer (YOKOGAWA, AQ6375C) analyzes the output spectrum, and a 10 GHz electro-photonic detector (CONQUER, KG-PD-10G-FP) records the time domain waveform, which is then analyzed with a 1 GHz oscilloscope (Tektronix, MSO4104).

2.2 Mode conversion based on TAP-LPFG and AIFG

Two kinds of all-fiber mode converters are utilized to achieve efficient LP_{11} mode in the FMFs, which have different spectrum responses with unique advantages. First is the LPFG written in a TMF by CO_2 laser radiation to achieve broadband conversion from LP_{01} to LP_{11} mode. Figure 2a demonstrates the experimental transmission spectrum of the broadband LPFG with a mode conversion efficiency of –16 dB (97.49%) and a 3-dB bandwidth of 115 nm. Second is the AIFG fabricated in another kind of FMF, which exhibits dual-resonant LP_{11a} and LP_{11b} modes with a wavelength separation interval of ~30 nm, as shown in Figure 2b. Both fiber mode converters are exploited in this study to show their robust capability of mode controlling in the application of high-power MLFLs.

The refractive index change of the LPFG is induced by CO_2 laser radiation moving along the fiber point-by-point operating in a fiber fusing station (LZM-100). The index modulation, grating period, and numbers can be accurately controlled by optimizing the timed CO_2 laser exposure power and duration. The TMF (core/cladding diameter of 9.4/125 μm and index difference of 0.0086) is found at the wavelength of 1.5 μm that group velocities between core modes of LP_{01} and LP_{11} are matched, which also refers to the condition of dispersion TAP as described in [36]. The dispersion of four-vector eigenmodes of LP_{11} mode, including TE_{01}, TM_{01}, and HE_{21} (even and odd) is calculated by employing a finite element method (FEM) (Comsol Multiphysics). Mode conversion in LPFG can be obtained when the phase-matching condition $L_B = \lambda/\Delta n = \Lambda$ is satisfied and $\lambda_{res} = \Lambda \cdot \Delta n_{eff} = \Lambda \cdot (n_{eff}^{01} - n_{eff}^{11})$, where L_B is the beat length, λ_{res} is the resonance wavelength, and Λ is the grating period. Δn_{eff} represents the difference of the effective refractive indices of LP_{01} (n_{eff}^{01}) and LP_{11} (n_{eff}^{11}). The

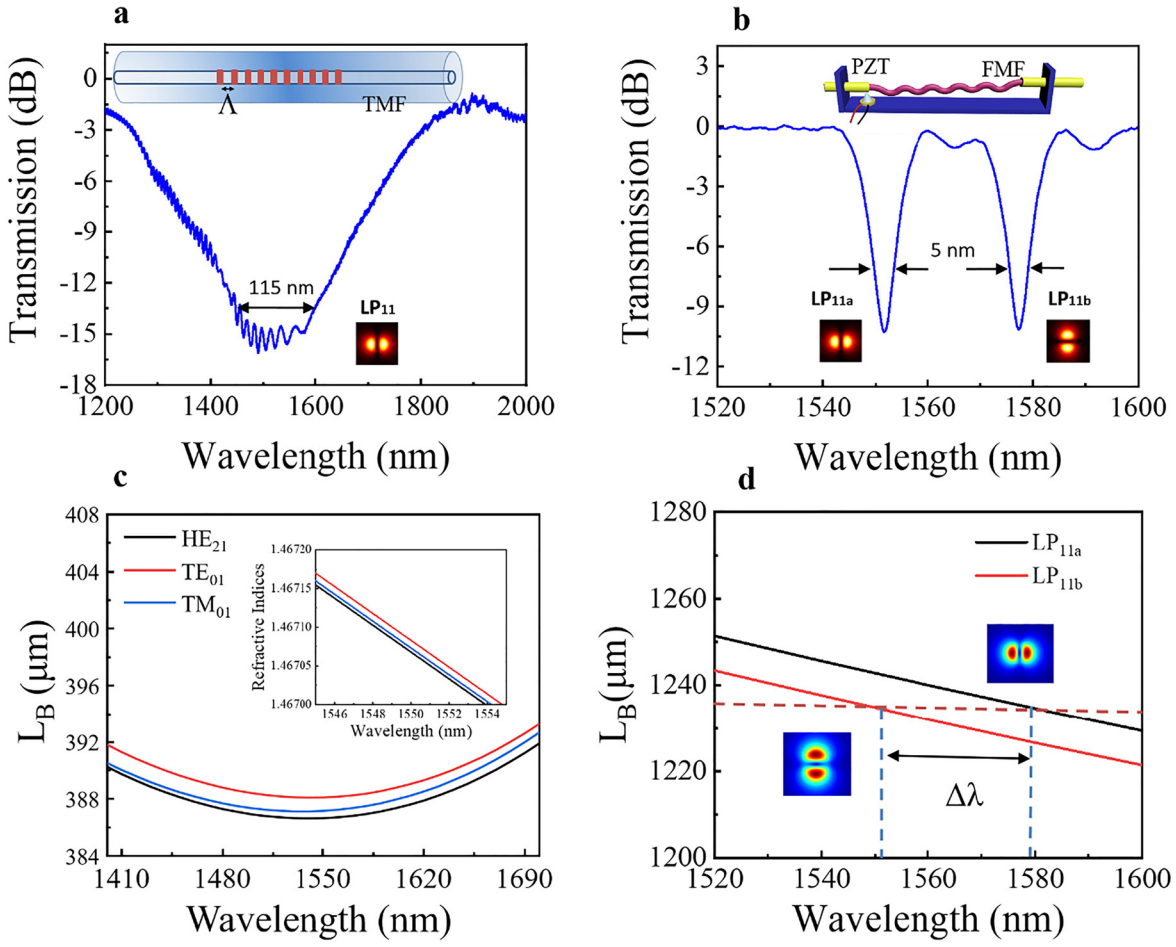

Figure 2: Transmission spectra and phase-matching curves for a TAP-LPFG and an AIFG.
(a) Broadband mode conversion and the inset is a schematic diagram of TAP-LPFG. (c) Beat length of LP_{11} eigenmodes (HE_{21}, TE_{01}, and TM_{01}) and the inset is refractive indices dependent on the wavelength. (b) Dual-resonant wavelengths in the transmission spectrum of an AIFG and the inset is the schematic diagram of the AIFG. (d) Beat length of LP_{11a} and LP_{11b} modes.

phase-matching curves (PMCs) for each vector modes are parabolic as shown in Figure 2c, indicating that there exists a broadband phase matching region at the extremum $[d(\Delta n)/d\lambda = 0]$. In other words, the same group velocities of these vector eigenmodes are achieved within the spectral region. The structured transmission spectrum is also seen due to the interference of vector eigenmodes.

An AIFG consists of a piezoceramic (PZT) and an adhered silica horn utilized for generating acoustic waves propagating along the FMF, which induces index change of periodic micro-bending fiber, and the basic structure of AIFG is shown in the inset of Figure 2b. The parameters of the FMF used in the AIFG are different from that of the LPFG. The core/cladding diameter is 18.4/125 μm and the refractive index difference is ~2.4×10^{-5}. The acousto-optic coupling length is generally tens of centimeters. The AIFG period can be calculated by the following formula: $\Lambda = \sqrt{(\pi R C_{ext}/f)}$, where R is the cladding radius of the FMF and f is the frequency of RF signal applied in the PZT to drive the acoustic wave, and $C_{ext} = 5760$ m/s is the velocity of the acoustic wave in optical fiber. The RF signal is amplified by a high-frequency-voltage amplifier (Aigtek: ATA-2022H).

The FMF used in the AIFG has been designed with slight ellipticity in the major and minor axes of the fiber. The ellipticity is defined as the ratio of the short to the long radius of the elliptical core. Compared with the circular-core fiber, a slightly elliptical-core FMF used in the AIFG will have new characteristics. The n_{eff} of scalar modes is calculated by using the FEM (Comsol Multiphysics) and two orthogonal LP_{11} scaler modes, corresponding to LP_{11a} and LP_{11b} respectively, are solved as shown in Figure 2d. Under the influence of core ellipticity, LP_{11a} and LP_{11b} modes transmitted in the elliptical-core FMF are no longer degenerate. Because of the phase-matching condition: $L_B = \lambda \cdot (n_{01} - n_{11a/b})^{-1}$, LP_{11a} and LP_{11b} modes with two

different beating lengths eventually lead to double resonance peaks in the transmission spectrum of the AIFG. Thus, the degeneration of LP_{11} mode to $LP_{11a/b}$ is induced by both optical and acoustic birefringence effects [37, 38].

Based on the vector mode theory of optical fiber, the elements of each LP set are formed by a linear combination of four eigenvector modes (TE_{01}, HE_{21}^{even}, HE_{21}^{odd}, and TM_{01}) with slightly different n_{eff} and LP_{11} mode is itself not stable and rotates if the fiber is disturbed. This instability may lead to LP_{11} mode with 90° rotated intensity patterns because of constructive and destructive interference. The linear superposition of vector modes is experimentally observed to be two-lobe patterns, similar to LP mode intensity of scalar model, which is named as $LP_{11a/b}^{x,y}$, according to the mode orientation (a or b) and polarization distribution (x or y). Thus, one can have a pair of orthogonal LP_{11} modes referred to as LP_{11a} and LP_{11b} in fibers, which are formed by the combination of four eigenvector modes:

$$LP_{11a} = LP_{11a}^{x} + LP_{11a}^{y} = TE_{01} + HE_{21}^{odd} + (TM_{01} + HE_{21}^{even}) \quad (1)$$

$$LP_{11b} = LP_{11b}^{x} + LP_{11b}^{y} = TM_{01} - HE_{21}^{even} + \left(TE_{01} - HE_{21}^{odd}\right) \quad (2)$$

In terms of two-lobe mode intensity distribution, LP_{11a} and LP_{11b} modes always remain to be orthogonal and have separated resonant wavelengths in the transmission spectrum of the AIFG using the elliptical-core fibers. It is noted that $LP_{11a/b}$ is not stably propagating mode inside the fiber due to the slightly different propagating constants of vector modes. However, stable $LP_{11a/b}$ can be directly delivered out of the fiber once the fiber laser and the AIFG are fixed. Moreover, a phase difference of "$\pi/2$" can be induced to the eigenvector modes by adjusting the angle of a QWP and a polarizer appropriately, and corresponding OAM mode can be observed in the experiment.

2.3 Method of mode control in first-order Poincaré sphere

Four vector eigenmodes of LP_{11} mode, including TE_{01}, TM_{01}, and HE_{21} (even and odd) are featured as the inhomogeneous polarization states with annular intensity profiles. In 1999, M. J. Padgett and J. Courtial [34] innovatively propose an equivalent higher-order Poincaré sphere to describe the evolution of LP_{11} mode in fiber, in which light carrying the first-order OAM positions on the poles and two-lobe LP modes along the equator. The different polarization states of LP modes can be regarded as a point located on the Poincaré sphere. The mode evolution and polarization transformation of a spatial light field by using a QWP and a polarizer were investigated theoretically [34]. Any point on the Poincaré sphere can be described as the superposition of two orthogonal modes, which can be written with Jones vector [39]:

$$|LP_{11a}| = \begin{bmatrix} 1 \\ 0 \end{bmatrix}, \ |LP_{11b}| = \begin{bmatrix} 0 \\ 1 \end{bmatrix} \quad (3)$$

$$|E_0| = A|LP_{11a}| + e^{i\varphi}B|LP_{11b}| = \begin{bmatrix} A \\ e^{i\varphi}B \end{bmatrix} \quad (4)$$

where A and B are normalized intensity of LP_{11a} and LP_{11b} modes ($A^2 + B^2 = 1$), respectively. φ means the phase difference between two orthogonal modes.

As shown in Figure 1a, θ_1 is the angle between the fast axis of the QWP and the x-axis and θ_2 is the polarizer selecting the polarization, which determines the azimuthal and polar angles in the sphere. The Jones matrix can be expressed as:

$$H(\theta_1, \theta_2) = H_{pol}(\theta_2) \times H_{QWP}(\theta_1) \quad (5)$$

$H_{QWP}(\theta_1)$ and $H_{pol}(\theta_2)$ are the Jones matrix of the QWP and the polarizer [40]:

$$H_{QWP}(\theta_1) = e^{-i\pi/4}\begin{bmatrix} \cos^2\theta_1 + i\sin^2\theta_1 & (1-i)\sin\theta_1\cos\theta_1 \\ (1-i)\sin\theta_1\cos\theta_1 & \sin^2\theta_1 + i\cos^2\theta_1 \end{bmatrix} \quad (6)$$

$$H_{pol}(\theta_2) = \begin{bmatrix} \cos^2\theta_2 & \sin\theta_2\cos\theta_2 \\ \sin\theta_2\cos\theta_2 & \sin^2\theta_2 \end{bmatrix} \quad (7)$$

$$|E_{out}| = H(\theta_1, \theta_2) \times |E_0| \quad (8)$$

where $\theta_1 \in [0, \pi]$ and $\theta_2 \in [0, \pi]$. When the phase difference between two decomposed orthogonal modes equals to $\pm\pi/2$, an OAM beam can be obtained, when $|\theta_1 - \theta_2| = \pi/4\,(3\pi/4)$.

In order to verify the QWP effect on the polarization state, it is assumed that the transmission axis of the polarizer is parallel with the optical axis of input mode, which means $\theta_2 = 0$. Figure 3a shows the mode patterns and their positions on the first-order Poincaré sphere for the LP_{11} mode group. The equator represents the standard LP_{11} mode in different directions. Two poles represent the right and left helical phase annular beams regarded as OAM_{+1} and OAM_{-1}, respectively. Figure 3b shows that along the longitude line of the PS from number 1 to 8, the mode intensity profile changes from LP_{11} mode to OAM mode patterns, and back to LP_{11} mode with θ_1 of 0, $\pi/8$, $\pi/4$, $3\pi/8$, $\pi/2$, $5\pi/8$, $3\pi/4$ and $7\pi/8$.

As shown in Figure 4, the observed modes and reference patterns output based on the LPFG and AIFG from the QWP and the polarizer can be controlled by changing θ_1.

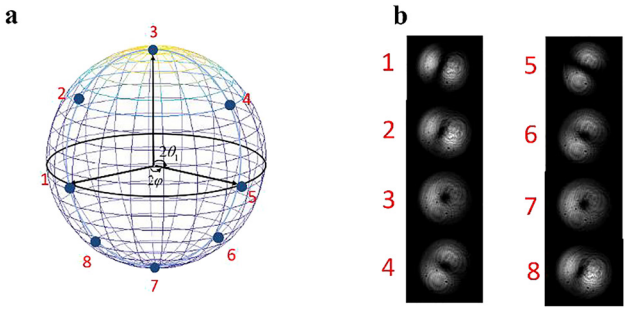

Figure 3: (a) Equivalent first-order Poincaré sphere combing with Jones vectors representation. (b) The mode patterns of specific points in a period on this sphere surface.

The evolution from LP_{11} mode to OAM mode can be observed when θ_1 changes from 0 to $\pi/4$, and then back to LP_{11} mode when θ_1 changes from $\pi/4$ to $\pi/2$. Therefore, the experimental results are in good agreement with the theory in Figure 3. Thus, the output from the DSR mode-locked laser can be regulated precisely by using a QWP and polarizer.

3 Results

3.1 MLFL with vortex mode output based on intra- and extra-cavity LPFG

The vortex modes with $OAM_{\pm1}$ are obtained by combining different vector eigenmodes with a $\pi/2$ phase difference. In the TAP-LPFG, the broadband conversion is due to the fact that each eigenmode have approximately the same L_B and the same group velocities around the resonance wavelength. Therefore, stable OVB can oscillate in the FMF part of the hybrid mode-locked cavity.

Firstly, in the experimental setup of Figure 1b, the TAP-LPFG acts as an LP_{01}–LP_{11} mode converter. An extra-cavity mode conversion by using the same LPFG has been done as shown in Figure 1c. Figure 5a shows a single rectangular pulse emitting from the MLFL, which is a typical mode-locked pulse in the DSR regime. The pulse amplitude keeps at a constant level as the pump power increases. It is also noted that the noise-like pulse (NLP) is a rectangular pulse, which is very similar to the DSR pulse [41]. However, the NLP is a wave packet consisting of many sub-pulses in sub-picoseconds while the DSR pulse is a single pulse without additional pulse components. We cannot observe any pulses on top of the noise level according to an autocorrelation (AC) with a scan range of 100 ps (the inset of Figure 5a). This verifies that the MLFL in this paper works in the DSR regime.

In order to compare the extra-cavity OVB output, an intra-cavity mode conversion has been done as shown in Figure 1b. The TAP-LPFG can also propagate forward LP_{11} in the TMF and couple back the reflected LP_{01} mode for light oscillation inside the cavity. The group velocities between core modes of LP_{01} and LP_{11} modes in the TAP-LPFG are matched, which leads to the possibility of optical vortex pulses oscillating inside the cavity. The transmitted LP_{11} and OVB from the output mirror 2 are detected and captured by a CCD. Meanwhile, with the adjustment of polarization state and phase difference addition controlled by the PCs inside the cavity, OVB is obtained in Figure 5b, which shows the output spectrum of the DSR mode-locked pulse and the inset is the intensity profile of the OVB. As shown in Figure 5b and c, the central wavelength of intra-cavity OVB mode-locked pulse locates at 1566 nm, and the 3-dB bandwidth is measured to be 8.18 nm, while the central wavelength of extra-cavity vortex conversion locates at 1610 nm, and the 3-dB bandwidth is measured to be 21 nm. Because of the

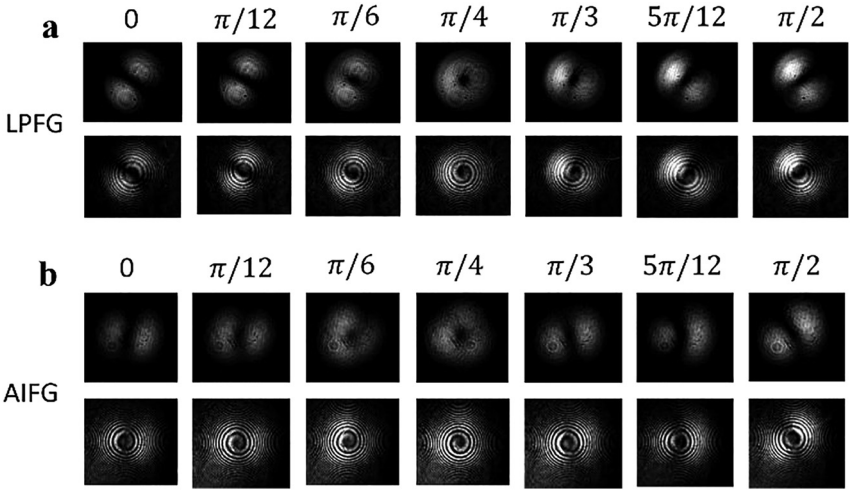

Figure 4: The mode and reference patterns of OAM mode output for θ_1 from 0 to $\pi/2$ based on (a) LPFG and (b) AIFG.

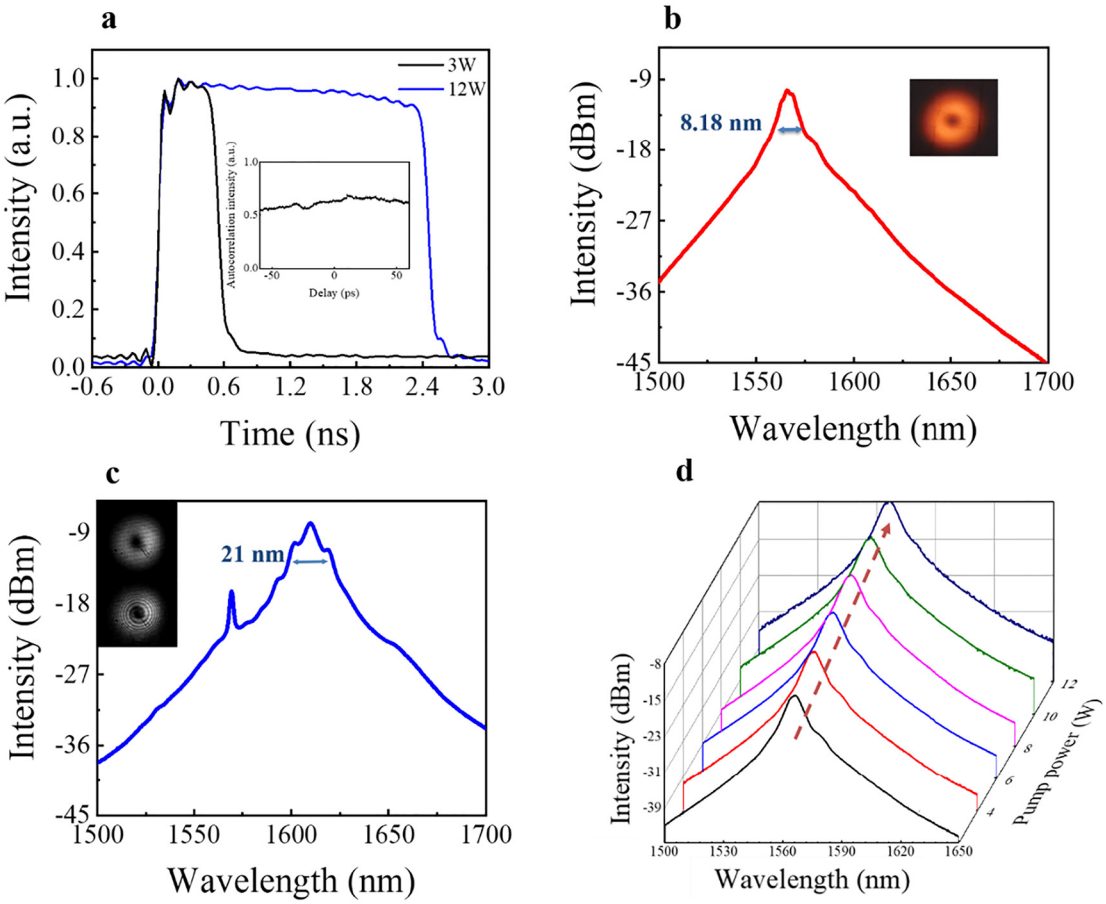

Figure 5: (a) The temporal profile of single DSR pulse (inset: autocorrelation trace). DSR mode-locking output spectra using the TAP-LPFG of (b) intra-cavity and (c) extra-cavity OVB and the insets are output OVB profiles. (d) The optical spectral evolution OVB mode from intra-cavity DSR MLFL as the pump power increases.

higher reflectivity of the fiber loop mirror than that of the fiber end face, the light intensity inside the laser cavity is larger, the center wavelength of the extra-cavity vortex pulse is red-shifted from 1566 nm (still see a small peak) to 1610 nm due to the secondary absorption of the gain fiber. The results indicate that broadband mode conversion within C-band with high efficiency is achieved by using the same LPFG. Figure 5d shows the output spectra of intra-cavity vortex pulses. Although the spectral intensity increases as the pump power increases, while their spectral profiles and widths are independent. This result shows the typical properties of DSR mode-locked pulses.

Compared with the OVB of fundamental mode soliton transformation outside the cavity, the intra-cavity OVB oscillation can avoid the interference of external factors, which further explains the spatiotemporal effect of higher-order modes in MLFLs.

Figure 6a describes the variation of output power against the pump power in mode-locked pulses of intra-cavity OVBs. The output power grows linearly with the pump power. The maximum average power of output 2 is 3.21 W with an efficiency slope of 26.75% and the maximum average power of output 1 is 416 mW, which is limited by the available pump power. The pulse peak powers of intra-cavity OVB are calculated as shown in Figure 6b. As increasing the pump power, the peak power region tends to a saturated power of ~105 W, which means that the single soliton of MLFL in the DSR regime can stand infinitely large energy without pulse breaking due to the strong peak-power-clamping effect in the 5/95 fiber loop mirror of a long length [42]. Figure 6c shows the evolution of the intra-cavity pulse width from 0.76 to 2.15 ns versus pump power. The growth rate of pulse width is slow at the first stage and becomes fast because the pulse peak power increases at first but then remains constant under the effect of the peak power-clamping effect [42].

Figure 7a shows the pulse shape evolution for the increased pump powers, which is in good agreement with the features of the DSR MLFL reported previously. Figure 7b and c show the pulse trains of LP_{11} mode with a repetition

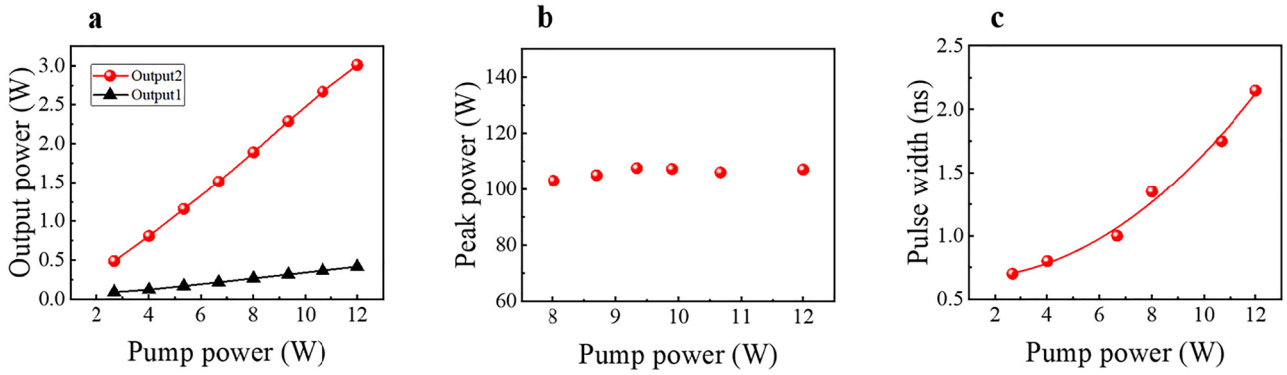

Figure 6: Intra-cavity DSR mode-locking output using the TAP-LPFG of (a) average output power, (b) peak power, and (c) pulse width as the function of pump power.

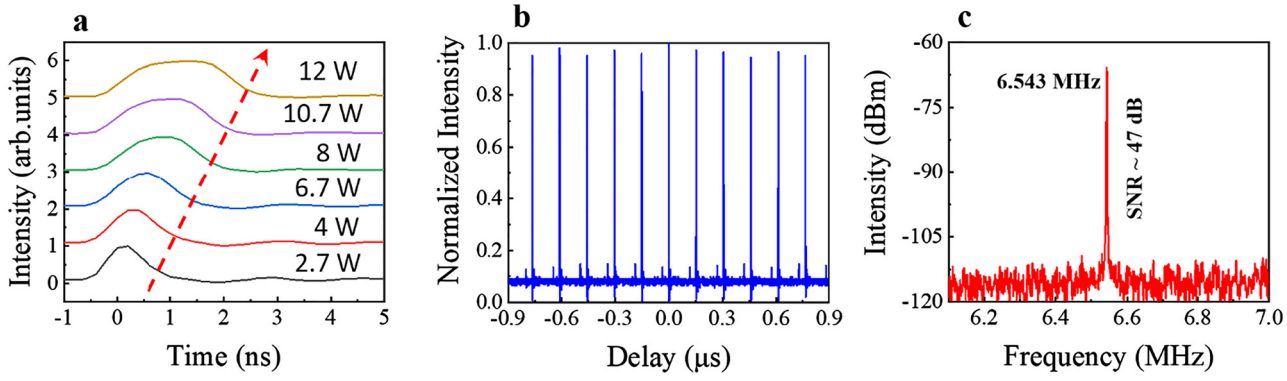

Figure 7: (a) Pulse shape evolution for the pump power of 2.7, 4, 6.7, 8, 10.7, and 12 W. (b) Mode-locking pulsed trace of intra-cavity OVB. (c) The RF spectrum at the fundamental frequency of OVB.

rate of 6.543 MHz and the signal-to-noise ratio (SNR) is about 47 dB.

3.2 MLFL with LP mode switching output

Secondly, the AIFG is used in the same experimental setup as shown in Figure 1a, which aims to achieve LP_{11} mode switching of the DSR mode-locked pulses. The transmission spectra of the AIFG used inside the cavity are shown in Figure 8a. To achieve LP_{01}–LP_{11a} (LP_{01}–LP_{11b}) mode conversion, the RF frequency is set to 745.6 kHz (732.6 kHz) for mode-locking laser emission at a wavelength of 1567 nm. Thus, based on the scheme, LP_{11a} and LP_{11b} modes are separately converted at the same wavelength by applying different RF frequencies. The length of the FMF without the coating layer is 0.45-m-long, which is the acousto-optic coupling region. When the voltage amplitude applied to the PZT is 46.5 and 55 V, the coupling efficiencies of LP_{01} mode to LP_{11a} and LP_{11b} modes can both reach 14 dB (~96%). Therefore, there are three mode-locked pulses of LP_{01}, LP_{11a}, and LP_{11b} modes dependent on the working states of the AIFG, which can be easily controlled by changing the frequencies of RF signals.

As shown in Figure 8b, the AIFG is just the FMF itself when the RF signal is turned off. LP_{01} mode spectrum of the mode-locked pulse is observed from Output 1. The central wavelength locates at 1566.82 nm and the 3-dB bandwidth is measured to be 10.21 nm. By modulating RF frequencies, the LP_{11a} mode and LP_{11b} mode spectrum are observed at the same lasing wavelength. The central wavelength of them is located at 1566.67 nm, and the 3-dB bandwidth is measured to be 8.83 and 9.13 nm, respectively. The 3-dB bandwidth of $LP_{11a/b}$ mode spectra becomes narrower than that of LP_{01} mode because of the filtering characteristics of the AIFG. The 3-dB bandwidth of AIFG can achieve ~10 nm when the transmission depth is around –10 dB. Therefore, most of the LP_{01} modes can be converted to higher-order modes.

Figure 9a shows the output spectra of LP_{11a} mode as the pump power increases. It is seen that although the spectral

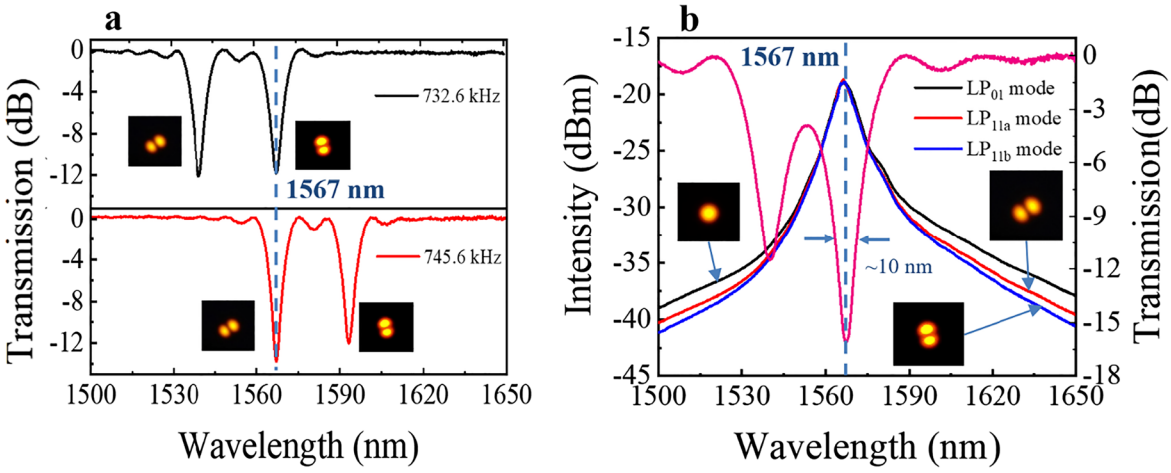

Figure 8: (a) The dual-resonant transmission spectra of the AIFG in the cavity. (b) Optical spectra of mode-locking states of LP_{01}, LP_{11a}, and LP_{11b} modes.

intensity increases with the increase of pump power, the spectral profiles and widths are similar as the proof of the DSR mode-locking. While the pulse width of the DSR pulses dependent on the pump power is also shown in Figure 9b, which shows that the pulse width of $LP_{11a/b}$ mode is narrower than that of LP_{01} mode at the same pump power. Figure 9c shows that the fiber laser operates in the continuous-wave (CW) state when the pump power is less than 1.7 W. Stable mode-locking pulses can be achieved as the pump power is progressively increased. The mode-

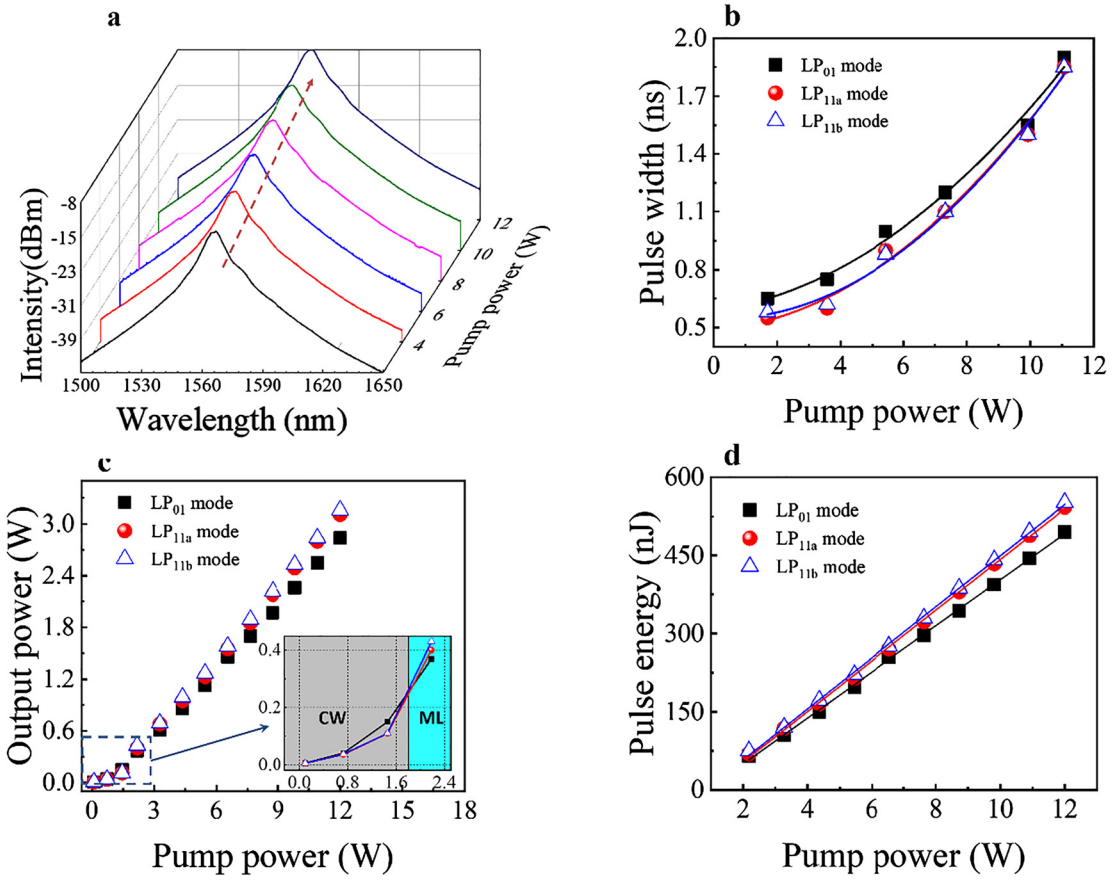

Figure 9: (a) The optical spectral evolution of LP_{11a} mode, (b) pulse width, (c) average output power of output 2, and (d) pulse energy as the pump power increases.

locked pulses of $LP_{11a/b}$ (LP_{01}) modes in the DSR regime enable a maximum average power of 3.0 W (2.8 W) with an efficiency slope of 25% (23.3%) as shown in Figure 9c. When the fiber laser works in the CW state, the output power of the LP_{01} mode is larger than that of $LP_{11a/b}$ modes. While the laser runs in the mode-locked state, the output power of the $LP_{11a/b}$ mode is greater than that of LP_{01} mode due to the smaller energy of a DSR soliton and narrower pulse duration. However, due to its nonuniform mode energy distribution, the reflectivity of output 2 to $LP_{11a/b}$ mode will be less than that of LP_{01} mode, which leads to the higher output power of $LP_{11a/b}$ mode. The pulse energy is calculated by using the measured average power. The pulse energy linearly increases from 65 to 500 nJ with the pump power increases from 2.2 to 12 W as shown in Figure 9d.

The evolution of pulse duration dependent on pump power is depicted for LP_{01} and $LP_{11a/b}$ in the DSR mode-locked region as shown in Figure 10a1–a3. When the pump power increases from 1.7 to 11.1 W, the pulse amplitudes remain constant and the pulse width increases gradually, which is consistent with the characteristics of DSR mode-locked pulses. Figure 10b1–b3 show the pulse trains of mode-locked LP_{01} and $LP_{11a/b}$ modes, which all have a repetition rate of 5.731 MHz because the cavity length of the laser remains unchanged during the switching process. Figure 10c1–c3 show the RF spectra of the output DSR mode-locked pulses of LP_{01} and $LP_{11a/b}$ modes when the peaks of the fundamental frequency are located at the cavity repetition rate of 5.731 MHz. The SNR of LP_{01} ($LP_{11a/b}$) mode is about 54 dB (53 dB).

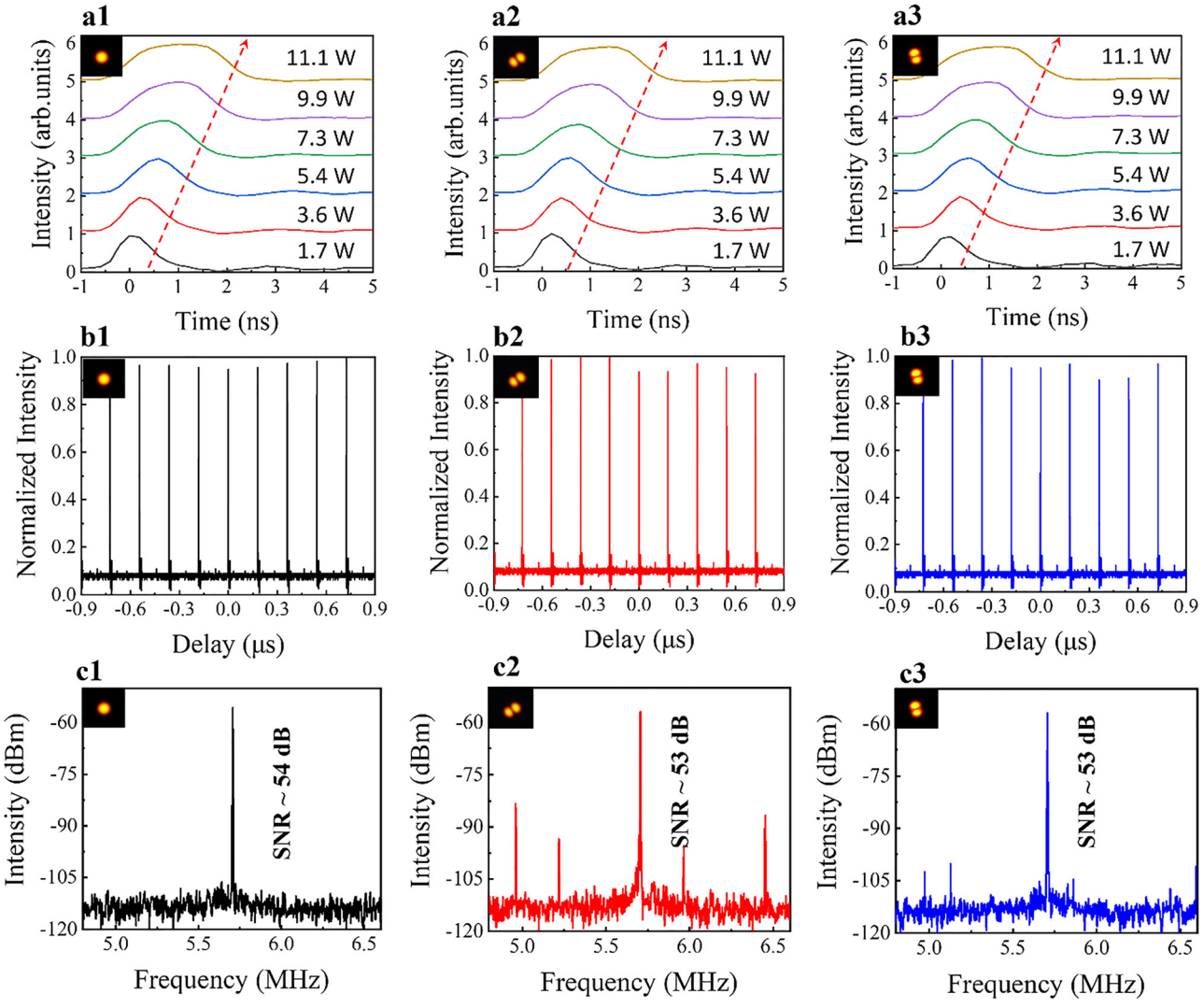

Figure 10: The pulse width as the pump power increases.
Pulse shape evolution for the pump powers of (a1) LP_{01} mode, (a2) LP_{11a} mode, and (a3) LP_{11b} mode. (b1)–(b3) Typical ML pulsed traces and (c1)–(c3) RF spectra at the fundamental frequency of LP_{01} and $LP_{11a/b}$ modes.

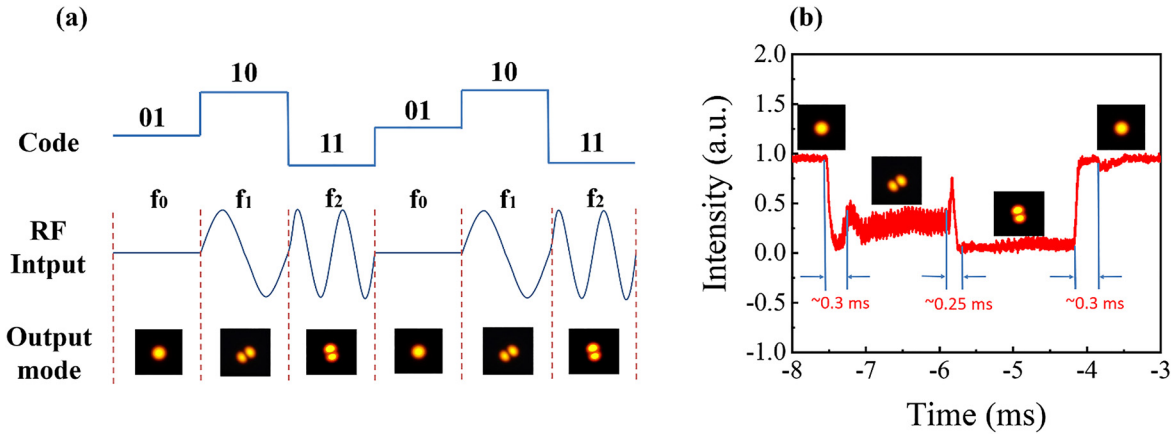

Figure 11: (a) The transverse mode with real-time switching can be modulated by the AIFG. (b) The speed of mode switching from LP_{01} mode to LP_{11a} (LP_{11b}).

When the lasing wavelength is around 1567 nm and the applied RF signal is set to f_1 (745.6 kHz) or f_2 (732.6 kHz), the laser operates at the state of LP_{11a} or LP_{11b} mode, respectively. To obtain a spatial mode switching in an MLFL, the applied RF signal is modulated via a frequency shift keying (FSK) method, which provides a periodic frequency modulation way for controlling the mode switching process. It is well noted that three mode-locked states always recover during the spatial mode switching between LP_{01}, LP_{11a}, and LP_{11b} modes. As shown in Figure 11a, the RF signal applied on the AIFG can be modulated by the binary codes such as 01, 10, and 11, which correspond to the RF frequencies of f_0 (nonresonant), f_1 (745.6 kHz), and f_2 (732.6 kHz). The output spatial modes are also dynamically switched at a speed of ~0.3 ms as shown in Figure 11b. Therefore, fast $LP_{11a/b}$ mode switching by using the FSK sequence provides a good application prospect in the field of programmable optical devices.

4 Conclusion

In this work, we have experimentally demonstrated Watt-level average-power HOM mode-locked pulses in the DSR regime by introducing two kinds of all-fiber mode converters: LPFG and AIFG. The controllable HOMs generation of high-energy pulses has great implications in the study of spatially mode-locking mechanism and ultrashort laser applications. We experimentally fabricated TAP-LPFG centered at 1550 nm covering a 3-dB bandwidth of ~115 nm by a CO_2 laser, which works near the dispersion TAP. It is found that the group velocities between the fundamental mode and LP_{11} eigenmodes are matched, which supports vortex soliton oscillation with a wide bandwidth. At the maximum pump power, the generated pulses have an average output power of 3.2 W with an efficiency slope of 26.75%; a dual-resonant AIFG is inserted in the same DSR MLFL with the function of fast switching (~0.3 ms) in LP_{01}, LP_{11a}, and LP_{11b} modes. The maximum average power can reach 3.0 W with an efficiency slope of 25%. A QWP and a polarizer are employed at the output of fiber laser to achieve the output of controllable OVBs and LP_{11} mode based on the first-order Poincaré sphere.

This work demonstrated the switching dynamics of spatial modes and the model of the ternary programmable device based on a high-order MLFL in the DSR regime. It is believed that a more important application by using such kind of controllable high-energy pulses can be expected in light–matter interaction. In conclusion, all these findings will promote the development of a new class of strategies for studying high-energy mode-locked pulses.

Acknowledgments: X. Zeng acknowledges the support of the Program for Professor of Special Appointment (Eastern Scholar) at Shanghai Institutions of Higher Learning.
Author contributions: All the authors have accepted responsibility for the entire content of this submitted manuscript and approved submission.
Research funding: National Science Foundation of China (NSFC) (91750108, 61635006); Science and Technology Commission of Shanghai Municipality (STCSM) (20JC1415700); Open Research Fund of State Key Laboratory of Pulsed Power Laser Technology (SKL2020KF03); 111 Project (D20031).
Conflict of interest statement: The authors declare no conflicts of interest.

References

[1] R. Gattass and E. Mazur, "Femtosecond laser micromachining in transparent materials," *Nat. Photonics*, vol. 2, pp. 219–225, 2008.

[2] K. Özgören, B. Öktem, and S. Yilmaz, "83 W, 3.1 MHz, square-shaped, 1 ns-pulsed all-fiber-integrated laser for micromachining," *Opt. Express*, vol. 19, pp. 17647–17652, 2011.

[3] G. A. Cranch, G. M. H. Flockhart, and C. K. Kirkendall, "Efficient fiber Bragg grating and fiber Fabry–Perot sensor multiplexing scheme using a broadband pulsed mode-locked laser," *J. Lightwave Technol.*, vol. 23, pp. 3798–3807, 2005.

[4] N. Nishizawa, Y. Chen, P. Hsiung, E. P. Ippen, and J. G. Fujimoto, "Real-time, ultrahigh-resolution, optical coherence tomography with an all-fiber, femtosecond fiber laser continuum at 1.5 μm," *Opt. Lett.*, vol. 29, p. 2846, 2004.

[5] W. Chang, A. Ankiewicz, J. M. Soto-Crespo, and N. Akhmediev, "Dissipative soliton resonances," *Phys. Rev. A*, vol. 78, p. 70, 2008.

[6] P. Grelu, W. Chang, A. Ankiewicz, Soto-Crespo, M. Jose, and N. Akhmediev, "Dissipative soliton resonance as a guideline for high-energy pulse laser oscillators," *J. Opt. Soc. Am. B.*, vol. 27, p. 2336, 2010.

[7] G. Herink, B. Jalali, C. Ropers, and D. R. Solli, "Resolving the build-up of femtosecond mode-locking with single-shot spectroscopy at 90 MHz frame rate," *Nat. Photonics*, vol. 10, pp. 321–326, 2016.

[8] J. Peng, M. Sorokina, S. Sugavanam, et al., "Real-time observation of dissipative soliton formation in nonlinear polarization rotation mode-locked fibre lasers," *Commun. Phys.*, vol. 1, p. 20, 2018.

[9] J. Peng, Z. Zhao, S. Boscolo, et al., "Breather Molecular Complexes in a Passively Mode-Locked Fibre Laser," *Laser Photonics Rev.*, vol. 15, p. 2000132, 2021.

[10] Y. Du, Z. Xu, and X. Shu, "Spatio-spectral dynamics of the pulsating dissipative solitons in a normal-dispersion fiber laser," *Opt. Lett.*, vol. 43, pp. 3602–3605, 2018.

[11] D. J. Richardson, J. M. Fini, and L. E. Nelson, "Space-division multiplexing in optical fibres," *Nat. Photonics*, vol. 7, pp. 354–362, 2013.

[12] H. R. Stuart, "Dispersive multiplexing in multimode optical fiber," *Science*, vol. 289, pp. 281–283, 2000.

[13] L. G. Wright, Z. M. Ziegler, P. M. Lushnikov, et al., "Multimode nonlinear fiber optics: massively parallel numerical solver, tutorial, and outlook," *IEEE J. Sel. Top. Quant. Electron.*, vol. 24, p. 5100516, 2018.

[14] L. G. Wright, D. N. Christodoulides, and F. W. Wise, "Spatiotemporal mode-locking in multimode fiber lasers," *Science*, vol. 358, pp. 94–97, 2017.

[15] W. H. Renninger and F. W. Wise, "Optical solitons in graded-index multimode fibres," *Nat. Commun.*, vol. 4, p. 1719, 2013.

[16] L. G. Wright, D. N. Christodoulides, and F. W. Wise, "Controllable spatiotemporal nonlinear effects in multimode fibres," *Nat. Photonics*, vol. 9, pp. 306–310, 2015.

[17] H. Qin, X. Xiao, P. Wang, and C. Yang, "Observation of soliton molecules in a spatiotemporal mode-locked multimode fiber laser," *Opt. Lett.*, vol. 43, pp. 1982–1985, 2018.

[18] L. Allen, M. W. Beijersbergen, R. Spreeuw, and J. Woerdman, "Orbital angular momentum of light and the transformation of Laguerre–Gaussian laser modes," *Phys. Rev. A*, vol. 45, pp. 8185–8189, 1992.

[19] C. Hnatovsky, V. G. Shvedov, W. Krolikowski, and A. V. Rode, "Materials processing with a tightly focused femtosecond laser vortex pulse," *Opt. Lett.*, vol. 35, pp. 3417–3419, 2010.

[20] M. Koyama, T. Hirose, M. Okida, K. Miyamoto, and T. Omatsu, "Power scaling of a picosecond vortex laser based on a stressed Yb-doped fiber amplifier," *Opt. Express*, vol. 19, pp. 994–999, 2011.

[21] K. Toyoda, K. Miyamoto, N. Aoki, R. Morita, and T. Omatsu, "Using optical vortex to control the chirality of twisted metal nanostructures," *Nano Lett.*, vol. 12, pp. 3645–3649, 2012.

[22] K. Toyoda, F. Takahashi, S. Takizawa, T. Yu, and T. Omatsu, "Transfer of light helicity to nanostructures," *Phys. Rev. Lett.*, vol. 110, p. 143603, 2013.

[23] F. Takahashi, K. Miyamoto, H. Hidai, K. Yamane, R. Morita, and T. Omatsu, "Picosecond optical vortex pulse illumination forms a monocrystalline silicon needle," *Sci. Rep.*, vol. 6, p. 21738, 2016.

[24] A. E. Willner, H. Huang, Y. Yan, et al., "Optical communications using orbital angular momentum beams," *Adv. Opt. Photonics*, vol. 7, pp. 66–106, 2015.

[25] L. Li, Q. Ruan, R. Yang, L. Zhao, and Z. Luo, "Bidirectional operation of 100 fs bound solitons in an ultra-compact mode-locked fiber laser," *Opt. Express*, vol. 24, p. 21020, 2016.

[26] J. Xu, L. Zhang, X. Liu, et al., "Dynamic vortex mode-switchable Brillouin/Erbium laser pumped by high-order mode," *Opt. Lett.*, vol. 46, pp. 468–471, 2021.

[27] J. Dong and K. S. Chiang, "Mode-locked fiber laser with transverse-mode selection based on a two-mode FBG," *IEEE Photonics Technol. Lett.*, vol. 26, pp. 1766–1769, 2014.

[28] T. Wang, F. Wang, F. Shi, et al., "Generation of femtosecond optical vortex beams in all-fiber mode-locked fiber laser using mode selective coupler," *J. Lightwave Technol.*, vol. 35, p. 2676241, 2017.

[29] B. Y. Kim, J. N. Blake, H. E. Engan, and H. J. Shaw, "All-fiber acousto-optic frequency shifter," *Opt. Lett.*, vol. 11, pp. 389–391, 1986.

[30] W. Zhang, K. Wei, L. Huang, et al., "Optical vortex generation with wavelength tunability based on an acoustically-induced fiber grating," *Opt. Express*, vol. 24, p. 19278, 2016.

[31] P. Z. Dashti, F. Alhassen, and H. P. Lee, "Transfer of orbital angular momentum between acoustic and optical vortices in optical fiber," *Phys. Rev. Lett.*, vol. 96, p. 043064, 2006.

[32] Y. Li, L. Huang, H. Han, et al., "Acousto-optic tunable ultrafast laser with vector-mode-coupling-induced polarization conversion," *Photonics Res.*, vol. 7, pp. 798–805, 2019.

[33] L. Zhang, J. Lu, L. Meng, et al., "A lower frequency shift based on mode conversion for optical heterodyne micro-vibration measurement," *J. Lightwave Technol.*, vol. 38, pp. 6057–6062, 2020.

[34] M. J. Padgett and J. Courtial, "Poincare-sphere equivalent for light beams containing orbital angular momentum," *Opt. Lett.*, vol. 24, p. 430, 1999.

[35] T. Du, Z. Luo, R. Yang, et al., "1.2-W average-power, 700-W peak-power, 100-ps dissipative soliton resonance in a compact Er:Yb co-doped double-clad fiber laser," *Opt. Lett.*, vol. 42, pp. 462–465, 2017.

[36] L. Teng, J. Lu, Y. He, L. Wang, and X. Zeng, "Vortex soliton oscillation in mode-locked laser based on broadband long period fiber grating," *Opt. Lett.*, vol. 46, pp. 2710–2713, 2021.

[37] J. Lu, L. Meng, S. Fan, et al., "Dynamic mode-switchable optical vortex beams using acousto-optic mode converter," *Opt. Lett.*, vol. 43, p. 5841, 2018.
[38] J. Lu, F. Shi, L. Meng, et al., "Real-time observation of vortex mode switching in a narrow-linewidth mode locked fiber laser," *Photonics Res.*, vol. 8, pp. 1204–1212, 2020.
[39] L. Yan, X. Zeng, M. Qi, L. Wei, and W. Jian, "Mode evolution in polarization maintain few mode fibers and applications in mode-division-multiplexing systems," in *Proc. SPIE 10019, Optoelectronic Devices and Integration VI, 100190N (31 October 2016)*.
[40] Y. Han, L. Chen, Y. Liu, et al., "Orbital angular momentum transition of light using a cylindrical vector beam," *Opt. Lett.*, vol. 43, pp. 2146–2149, 2018.
[41] O. Pottiez, B. Ibarra-Escamilla, E. Kuzin, et al., "Multiple noise-like pulsing of a figure-eight fibre laser," *Laser Phys.*, vol. 24, p. 15103, 2013.
[42] D. Li, D. Tang, L. Zhao, and D. Shen, "Mechanism of dissipative-soliton-resonance generation in passively mode-locked all-normal-dispersion fiber lasers," *J. Lightwave Technol.*, vol. 33, pp. 3781–3787, 2015.